Supplementary Information

Favorable Nucleation and Continuous Regulation Direct Uniform and Oblate Li Deposition

Chen Liu,[a] Shuting Sun,[a] Shan Jin,[a] Tianning Lin,[a] Fei Ding,[*b] Ruhong Li [*c] and Changsong Dai [*a]

[a] MIIT Key Laboratory of Critical Materials Technology for New Energy Conversion and Storage, School of Chemistry and Chemical Engineering, Harbin Institute of Technology, Harbin, 150001, China

[b] State Key Lab Reliability & Intelligence Electrical Equipment, School of Electrical Engineering, Hebei University of Technology, Tianjin 300132, China

[c] State Key Laboratory of Silicon Materials, School of Materials Science and Engineering, Zhejiang University, Hangzhou 310027, China

[*] Corresponding author (email: hilldingfei@163.com (Ding F); ruhong@zju.edu.cn (Li R); changsd@hit.edu.cn (Dai C))

EXPERIMENTAL SECTION

Preparation of CNT-ZIF-8 and CNT-ZnS-T. $Zn(NO_3)_2 \cdot 6H_2O$ (0.001 mol) and CNT (0.1 g) were mixed uniformly in methanol (20 mL), following by pouring the same volume of 2-methylimidazole (0.004 mol) methanol solution into the former.[1-3] The mixture was stirred for 10 min and then aged for 24 h. After washing, centrifugation, and drying, CNT-ZIF-8 could be obtained. Subsequently, the precursor was treated at high temperature with the sulfur-vapor atmosphere to process the chemical conversion from ZIF-8 to ZnS. The acquired material was recorded as CNT-ZnS-T (T is the sintering temperature). In addition, the comparative sample heat-treated in normal Ar atmosphere was denoted by CNT-ZIF-8-NS-T.

Characterization. X-ray diffraction technique (XRD, Bruker, D2 PHASER) was employed to reveal the variation of crystal composition and structure with the 2θ scope of 5-90°. Particularly, Kapton sealant served as the blocking layer while the sample was air sensitive. Lattice fringe/diffraction ring of the specimens were acquired by transmission electron microscope (TEM, FEI, Tecnai G2 F30). The basic morphological features were determined using scanning electron microscope (SEM, HITACHI, FEI Quanta SU8010 & ZEISS, SUPRA55). The vibration frequencies via the infrared tests (FTIR, Thermo Fisher, NICOLET IS50) were compared to intuitively illustrate the destruction of ZIF-8 structure and the existing groups after high temperature treatment. X-ray photoelectron spectroscopy (XPS, Thermo Fisher, ESCLAB 250Xi) was adopted to analyze the surface composition and binding states. For the observation involving the samples after cycling, the disassembled electrodes

were first rinsed with ethylene glycol dimethyl ether (DME) to avoid lithium salt residues and then placed in the Ar-filled glove box over 24 h to obtain fully dried samples.

Electrochemical Tests. The ZnS-rich matrix was prepared by casting the slurry which was mixed by CNT-ZnS-T, super P and carboxymethyl cellulose (CMC) with the mass ratio of 8:1:1 on a copper foil. The coating mass density on the copper foil was approximately 0.8-1.4 mg cm^{-2}. Coulombic efficiency tests of half cells were conducted at 0.5, 1 mA cm^{-2} with 1M LiTFSI, 2 wt% LiNO$_3$, DOL/DME (v:v, 1:1) as the electrolyte. When the half cells were measured at 5 mA cm^{-2}, 4M LiFSI, DME system was employed as the electrolyte. In addition, LiFePO$_4$ cathode (LFP) with the typical mass load of 4.5 mg cm^{-2} was paired with CNT-ZnS-T electrode after lithium deposition (10 mAh cm^{-2}) to examine the cycle stability of full cells. The experiments involving galvanostatic charge and discharge were carried out on the Neware battery tester. Electrochemical impedance spectroscopy (EIS) was collected by an electrochemical workstation (CHENHUA, CHI660E) in the frequency range of 10^5-10^{-2} Hz along with the amplitude of 5 mV.

Computational Methods. All items mentioned below were acquired based on density functional theory (DFT) calculation via the Vienna ab initio simulation package, adopting the projector augmented wave (PAW) approach.[4-5] The exchange-correlation functional was treated by the generalized gradient approximation (GGA) of Perdew-Burke-Ernzerhof (PBE).[6-7] The adsorption energies of a Li atom on pure Li, Li$_{1-x}$Zn$_x$, LiZn surface were calculated according to the following relationship:[8]

$$E_{ads} = E'_{A-Li} - E_A - E_{Li}$$

E_A, E_{Li} were the energies of pure Li/Li$_{1-x}$Zn$_x$/LiZn slab and isolated Li atom model separately and E'_{A-Li} corresponded to the energy of the Li adsorption model. The slab models were constructed by cleaving specific low-index planes and introducing a vacuum spacing of 15 Å in z direction. For the calculation of adsorption behavior, two layers of atoms at the bottom of the slab were fixed when the other layers were relaxed. The binding energy landscape of a Li atom on specific surfaces was obtained by scanning the binding energy on various adsorption sites. The diffusion energy barrier on specific slab was also studied by performing climbing image nudge elastic band (CI-NEB) strategy.[9] Several intermediate images were set according to the spacing between the initial and the final state. The energy cutoff was 450 eV while 2*2*1 k points centered at Gamma were applied for relevant calculations with the assistance of VASPKIT.[10] It was regarded as accomplishing optimization as the energy difference was less than 10^{-5} eV between two adjacent self-consistent iteration steps and the residual force for relaxed atoms was concurrently lower than 0.02 eV Å^{-1}. The visualization of adsorption configuration and diffusion profiles was realized through VESTA software.[11]
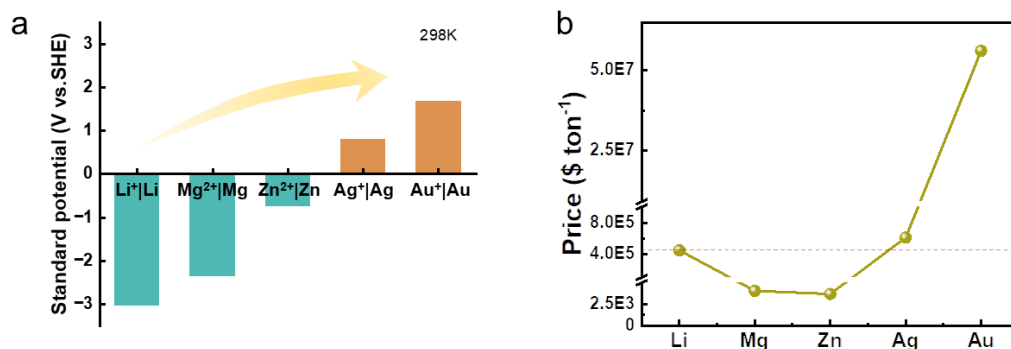
SUPPLEMENTARY FIGURES

Fig. S1 (a) Standard potentials of selected half-reactions at 298 K and (b) current price statistics of involved metals as of Aug. 2022, related data are collected from multiple web pages.

For Mg, Zn, Ag, Au, the three primary indicators to be examined are price, molar mass and redox stability. For Ag and Au, the manufacturing cost is more expensive and the higher mass (Ag: 108 g mol^{-1}; Au: 197 g mol^{-1}) also plays a disadvantage role in increasing the energy density. The comparison of price and mass makes the selected target focus on Mg and Zn. In terms of redox stability, metallic Mg is more prone to lose electrons which means that the electrode is more possible to passivate with the participation of Mg compared with Zn. Some literature has discussed that the passivation may cause a series of dilemmas such as low voltage platform and reduced cycling stability[12,13]. Besides, the highly reactive nature of Mg may even raise safety concerns. Hence, Zn is chosen as the main modified component considered in this research.
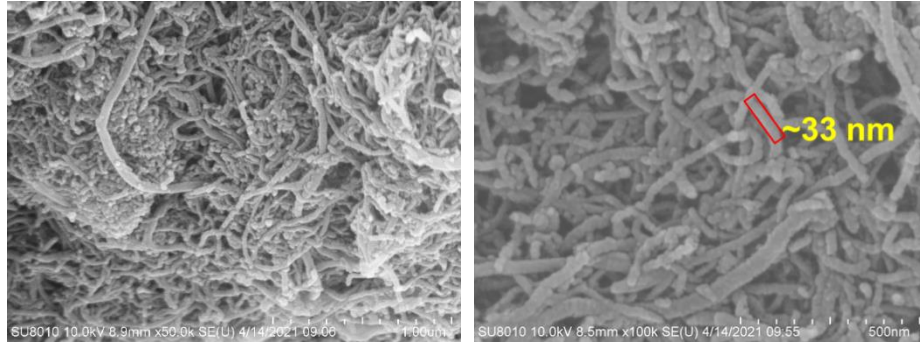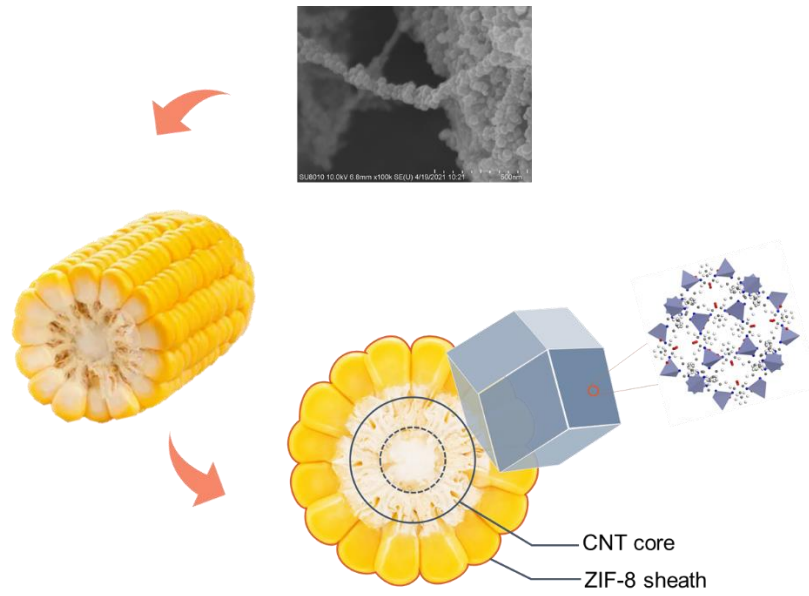
Fig. S2 SEM images of CNT.

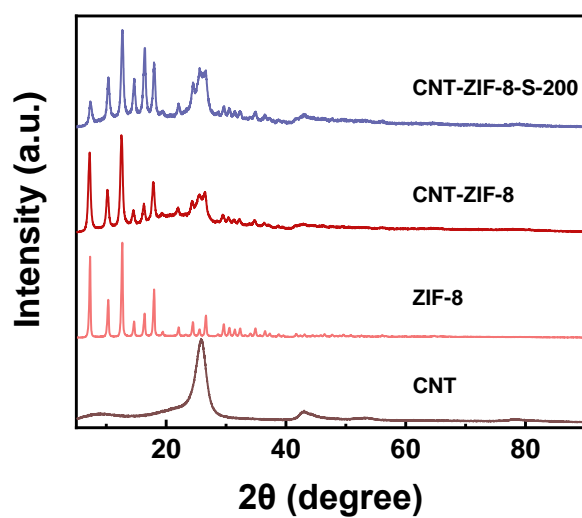**Fig. S3** Schematic illustration of CNT-ZIF-8.

Fig. S4 XRD patterns of CNT-ZIF-8-S-200, CNT-ZIF-8, ZIF-8 and CNT; CNT-ZIF-8-S-200 is

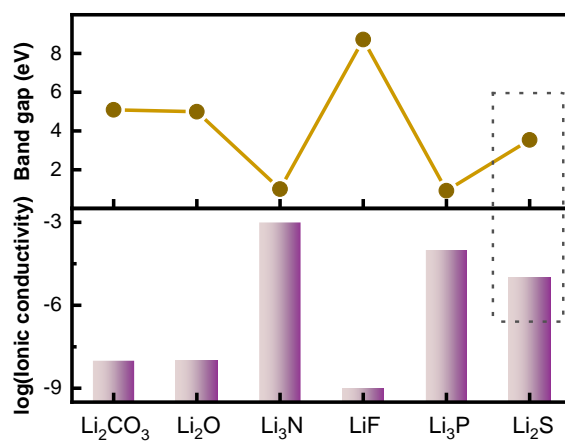obtained by a similar preparation method to CNT-ZnS-T at a lower temperature of 200 °C.

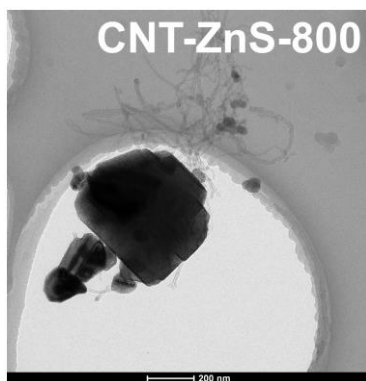**Fig. S5** Ionic conductivity and band gap comparison of common inorganic components in SEI.[14-17]
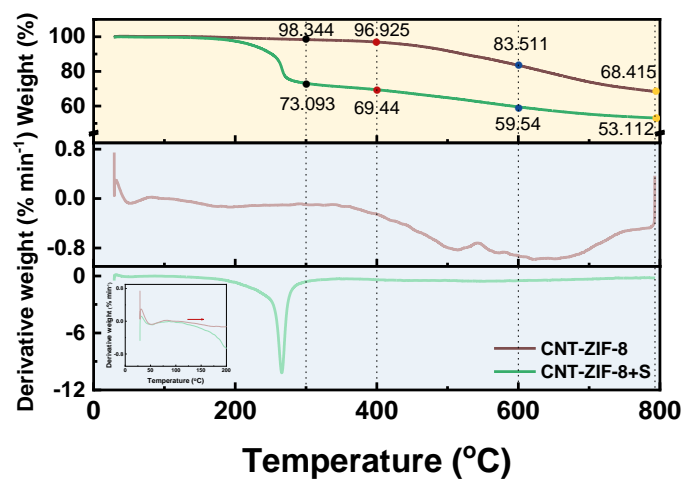
Fig. S6 TEM image of CNT-ZnS-800.

Fig. S7 Thermogravimetric analysis of CNT-ZIF-8 with/without sulfur at the temperature range of
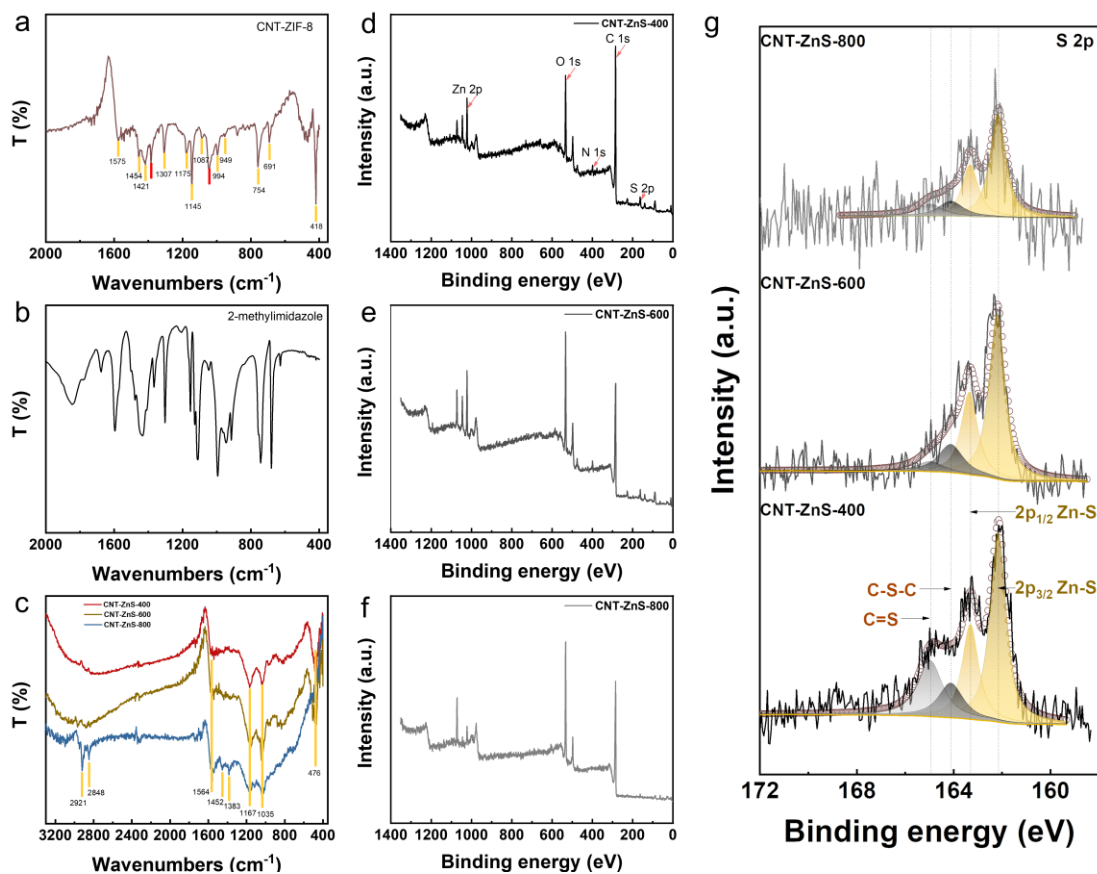
30-800 ℃.

Fig. S8 FTIR spectra of (a) CNT-ZIF-8, (b) 2-methylimidazole and (c) CNT-ZnS-T; XPS full spectra of (d) CNT-ZnS-400, (e) CNT-ZnS-600 and (f) CNT-ZnS-800; the detailed XPS spectra and fitting results of (g) S 2p of CNT-ZnS-T.
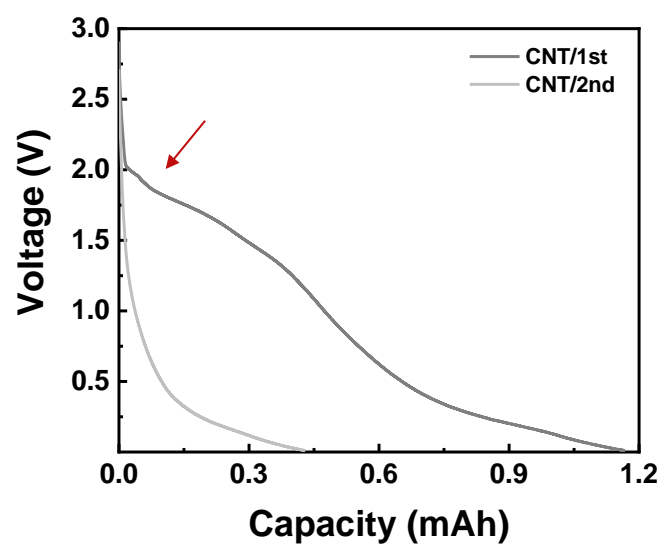
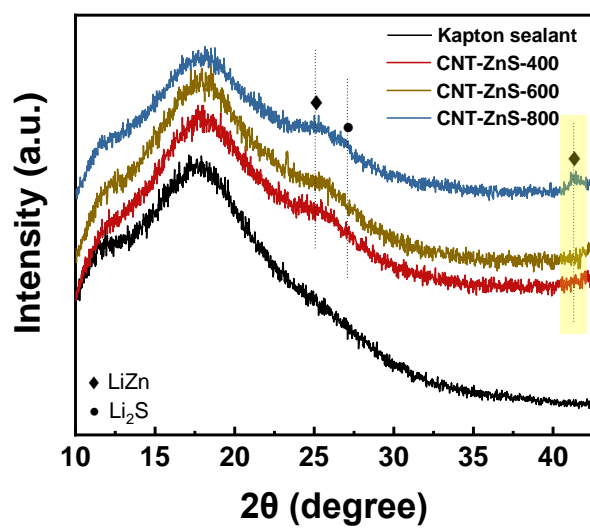**Fig. S9** Discharge curves of CNT|Li half cell.

Fig. S10 XRD patterns of CNT-ZnS-T with the existence of copper foil after activation.
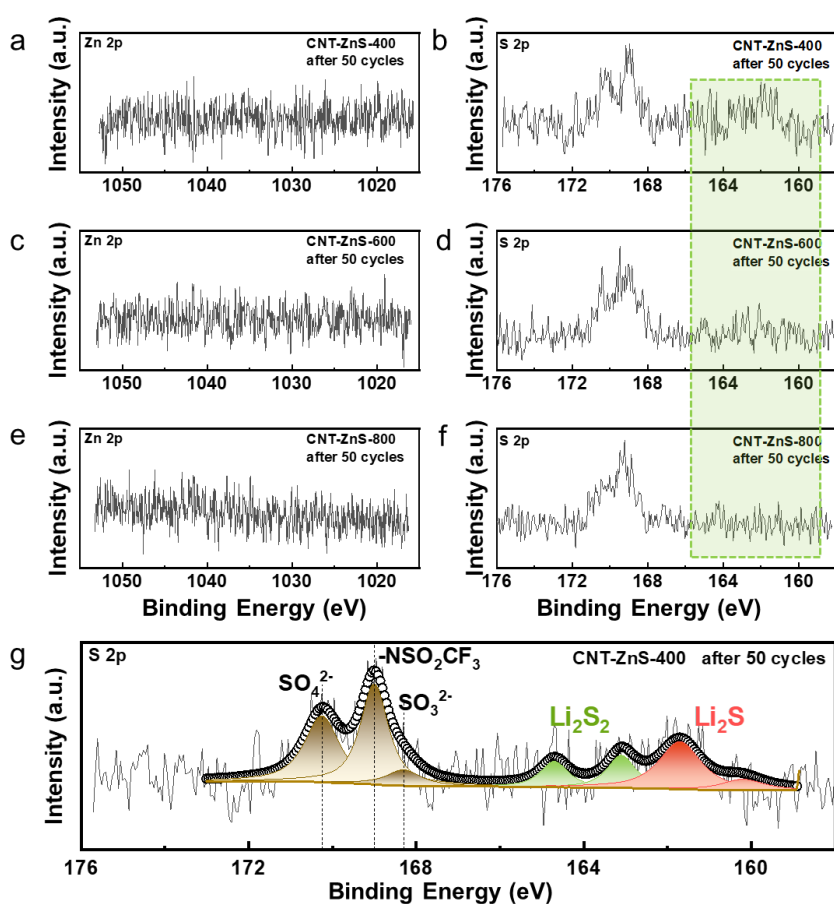
Fig. S11 XPS spectra of the electrodes after 50 cycles at 1 mA cm^{-2}. (a) Zn 2p and (b) S 2p profiles of CNT-ZnS-400, (c) Zn 2p and (d) S 2p profiles of CNT-ZnS-600, (e) Zn 2p and (f) S 2p profiles of CNT-ZnS-400; (g) the fitting results of (b), as a representative.

Fig. S11a-f present the high-resolution Zn 2p and S 2p spectra of CNT-ZnS-400, CNT-ZnS-600, CNT-ZnS-800 after 50 cycles at 1mA cm^{-2}, 1mAh cm^{-2}. In view of the distinct peak signals in S 2p spectra, deconvolution analysis is carried out with CNT-ZnS-400 as a representative (Fig. S11g). In the higher binding energy region, three peaks appeared at 170.3 eV, 169.0 eV, 168.3 eV separately correspond to SO$_4^{2-}$, -NSO$_2$CF$_3$ and SO$_3^{2-}$. The peaks at 160.2 eV and 161.7 eV are assigned to Li$_2$S while the neighboring peaks at 163.1 eV and 164.7 eV are allocated to Li$_2$S$_2$[15,18]. For CNT-

ZnS-T, the divergence between Zn 2p and S 2p spectra amply illustrates that LiZn primarily exists below Li_2S and this relative position is hardly interfered by the crystallinity of the precursor. In addition, the weakening of Li_2S signals when increasing sintering temperature originates from the interfacial instability/thickening caused by local aggregation, which is consistent with Fig. 3d.
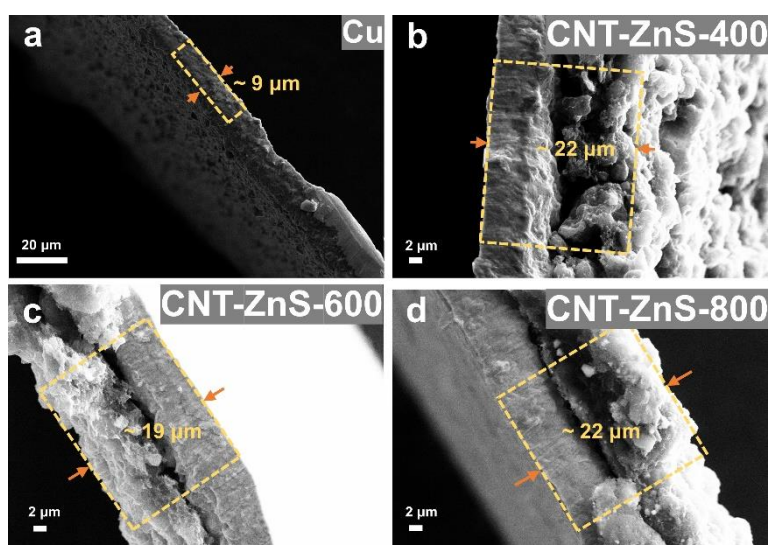

Fig. S12 The lateral views of (a) Cu, (b) CNT-ZnS-400, (c) CNT-ZnS-600 and (d) CNT-ZnS-800
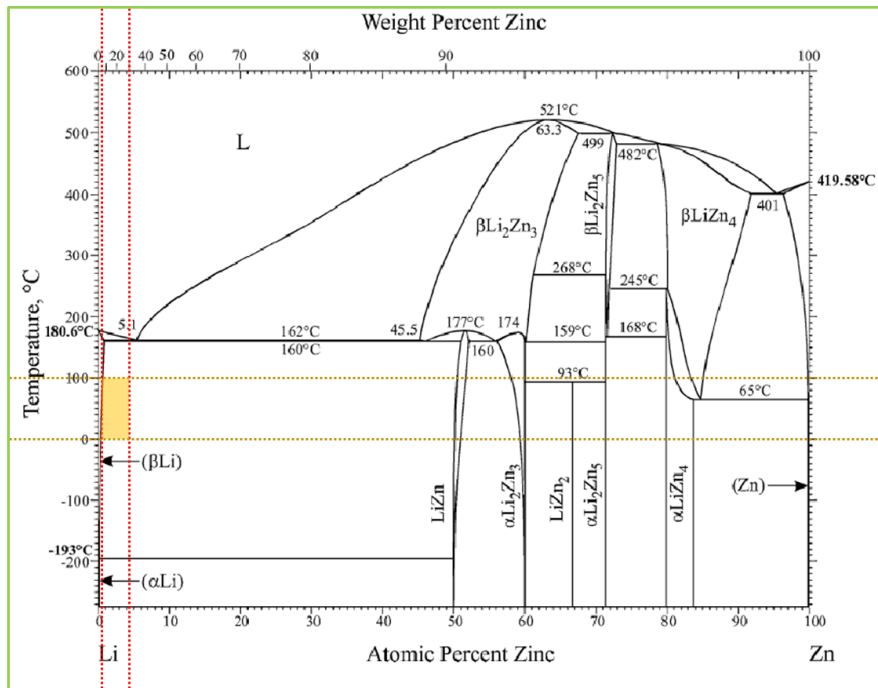
fresh electrodes.

Fig. S13 The phase diagram of Li-Zn, the yellow shadow points to involved region of common deposition capacity (1-10 mAh cm^{-2}) reported in the literature; the original diagram is gathered from FactSage.
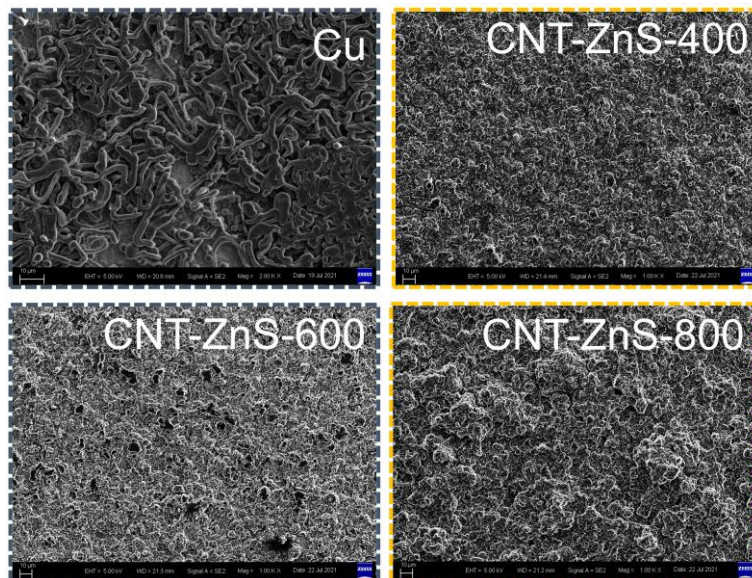

Fig. S14 SEM images with smaller magnification of (a) Cu, (b) CNT-ZnS-400, (c) CNT-ZnS-600 and (d) CNT-ZnS-800 after plating 1mAh cm^{-2} Li; scale bar: 10 μm.
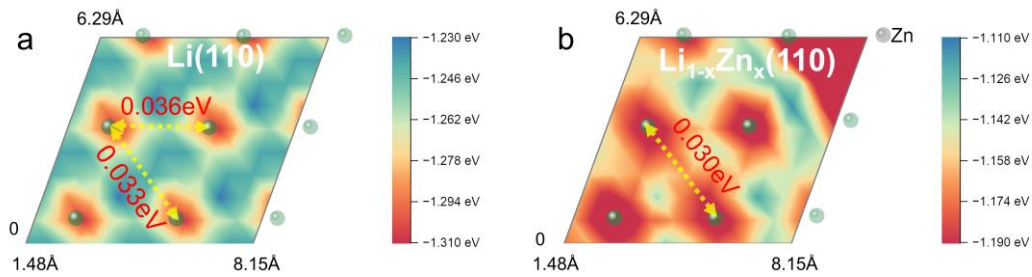
Fig. S15 The detailed binding energy landscape of a Li atom on (a) Li(110) and (b) $Li_{1-x}Zn_x$(110) surfaces, the green ball represents Li atom on the top layer and the grey ball represents Zn atom on the top layer.

The potential energy surfaces can also provide valuable information for possible diffusion paths of a Li atom on Li(110) and $Li_{1-x}Zn_x$(110) surfaces. Based on the potential energy surface of Li(110), we first choose two paths with approximate small energy changes for further evaluations and the calculation results of diffusion barriers are displayed in Fig. S15a. A similar path is selected for $Li_{1-x}Zn_x$(110), analogous to the diffusion path with lower energy barrier (0.033 eV) on Li(110). The corresponding diffusion energy barrier on $Li_{1-x}Zn_x$(110) drops to 0.030 eV. This comparison confirms that the substitution of Zn at the Li site can indeed bring tangible benefit on the acceleration of Li diffusion on the adjacent Li site. Worth mentioning, the diffusion path of a Li atom on LiZn(220) is determined according to the potential energy surface and literature reference.[19]
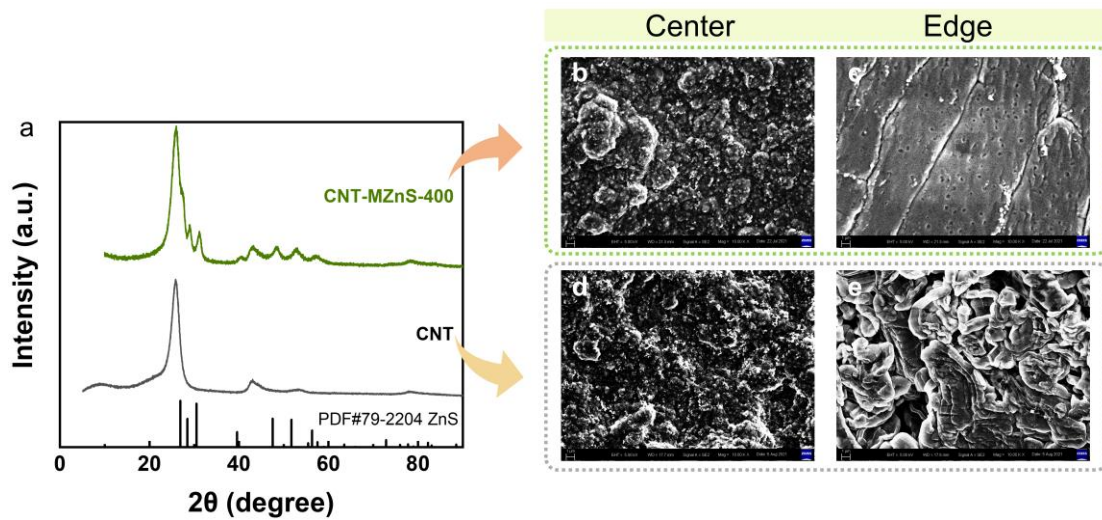
Fig. S16 (a) XRD patterns of CNT-MZnS-400 and CNT; the lithium deposition morphology of (b, c) CNT-MZnS-400 and (d, e) CNT with the plating capacity of 5 mAh cm^{-2}; scale bar: 1 μm. The fabrication of CNT-MZnS-400 consists of two main procedures: (1) simple mixing zinc chloride (ZnCl$_2$) and CNT; (2) sintering at 400 °C with the sulfur-vapor atmosphere.

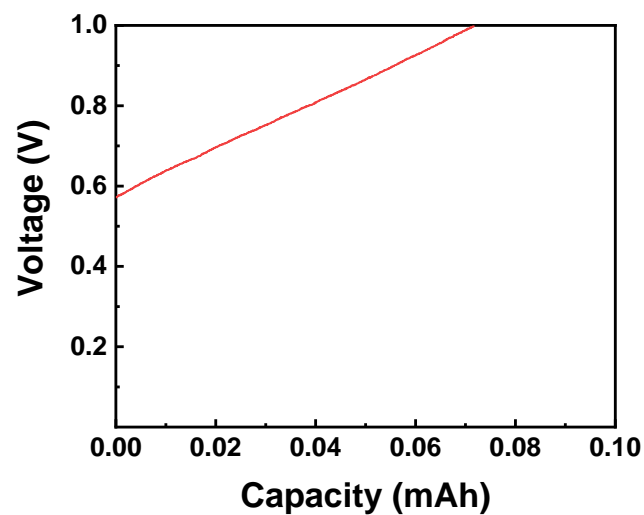**Fig. S17** The charge curve of the cell with CNT-ZnS-400 electrode after activation (3.0-0.01 V) as the cathode and Li foil as the anode between 0-1.0 V.
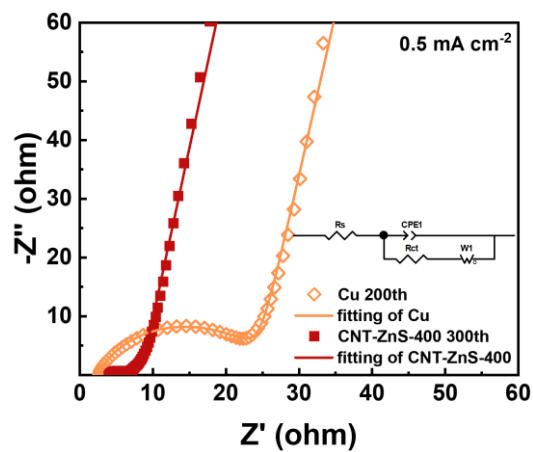
Fig. S18 EIS comparison of CNT-ZnS-400|Li and Cu|Li after cycles, the inset shows the

equivalent circuit.

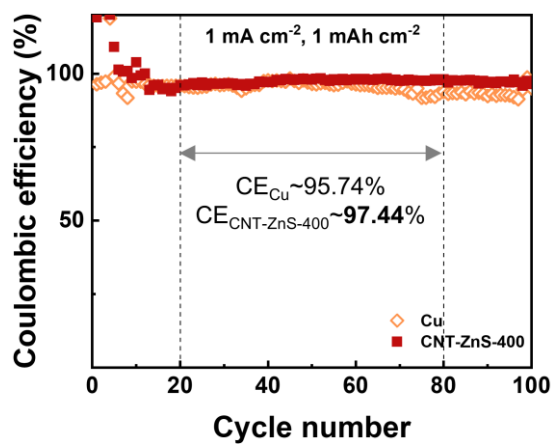**Fig. S19** Coulombic efficiency of CNT-ZnS-400|Li and Cu|Li cells at 1.0 mA cm^{-2}, 1.0 mAh cm^{-2}.
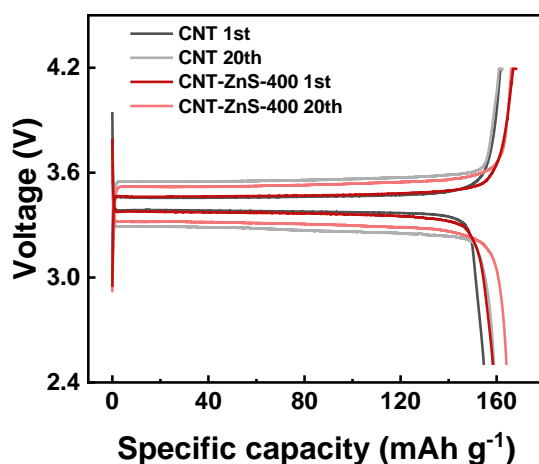
Fig. S20 The comparison of representative charge/discharge curves for CNT@Li|LFP and CNT-

ZnS-400@Li|LFP at 0.1C.

REFERENCES

1   S. Yan, K. Wang, Q. Wu, F. Zhou, Z. Lin, H. Song and Y. Shi, The fabrication of Co:ZnS/CoS$_2$ heterostructure nanowires with a superior hydrogen evolution performance, *Sustain. Energy Fuels*, 2019, **3**: 2771-2778.

2   D. Cao, W. Kang, W, Wang, K. Sun, Y. Wang, P. Ma and D. Sun, Okra-like Fe$_7$S$_8$/C@ZnS/N-C@C with core-double-shelled structures as robust and high-rate sodium anode, *Small*, 2020, **16**: 1907641.

3   F. Saadat, A. Alizadeh, M. Roudgar-Amoli and Z. Shariatinia, Exploring the influence of Zn$_2$SnO$_4$/ZIF-8 nanocomposite photoelectrodes on boosting efficiency of dye sensitized solar cells, *Ceram. Int.*, 2022, **48**: 21853-21864.

4   A. Jain, Y. Shin, K. A. Persson, Computational predictions of energy materials using density functional theory, *Nat. Rev. Mater.*, 2016, **1**: 15004.

5   R. Li, T. Chen, J. Liu, N. Jiang, G. Luo, F. Ding, Y. Du and C. Dai, Deciphering the role of cationic substitution towards highly stable polyanionic cathodes, *Energy Storage Mater.*, 2020, **29**: 223-234.

6   J. P. Perdew, K. Burke and M Ernzerhof, Generalized gradient approximation made simple, *Phys. Rev. Lett.*, 1996, **77**: 3865-3868.

7   Y. Liang, Y. Chen, X. Ke, Z. Zhang, W. Wu, G. Lin, Z. Zhou and Z. Shi, Coupling of triporosity and strong Au-Li interaction to enable dendrite-free lithium plating/stripping for long-life lithium metal anodes, *J. Mater. Chem. A*, 2020, **8**: 18094-18105.

8   J. Liu, T. Chen, R. Li, S. Shu, C. Liu, D. Mu, W. Wan, Z. Wang, J. Wei, S. Tian and C. Dai, Enhanced electrochemical performance of Li-S battery via structural transformation of N,O dual-doped carbon host material, *Electrochim. Acta*, 2021, **393**: 139070.

9   G. Henkelman, B. P. Uberuaga, H. Jónsson, A climbing image nudged elastic band method for finding saddle points and minimum energy paths, *J. Chem. Phys.*, 2000, **113**: 9901-9904.

10   V. Wang, N. Xu, J. Liu, G. Tang and W. Geng, VASPKIT: A user-friendly interface facilitating high-throughput computing and analysis using VASP code, *Comput. Phys. Commun.*, 2021, **267**: 108033.

11   K. Momma, F. Izumi, VESTA 3 for three-dimensional visualization of crystal, volumetric and morphology data, *J. Appl. Crystallogr.*, 2011, **44**: 1272-1276.

12   R. Li, Q. Liu, R. Zhang, Y. Li, Y. Ma, H. Huo, Y. Gao, P. Zuo, J. Wang and G. Yin, Achieving high-energy-density magnesium/sulfur battery via a passivation-free Mg-Li alloy anode, *Energy Storage Mater.*, 2022, **50**: 380-386.

13   M. N. Obrovac, V. L. Chevrier, Alloy negative electrodes for Li-ion batteries, *Chem. Rev.*, 2014, **114**: 11444-11502.

14   A. Jain, S. P. Ong, G. Hautier, W. Chen, W. D. Richards, S. Dacek, S. Cholia, D. Gunter, D. Skinner, G. Ceder and K. A. Persson, Commentary: The Materials Project: A materials genome approach to accelerating materials innovation, *APL Mater.*, 2013, **1**: 11002.

15   H. Chen, A. Pei, D. Lin, J. Xie, A. Yang, J. Xu, K, Lin, J. Wang, H. Wang, F. Shi, D. Boyle and Y. Cui, Uniform high ionic conducting lithium sulfide protection layer for stable lithium metal anode, *Adv. Energy Mater.*, 2019, **9**: 1900858.

16   W. Cao, Q. Li, X. Yu and H. Li, Controlling Li deposition below the interface, *eScience*, 2022, **2**: 47-78.

17   B. Hou, Y. Wang, Q. Ning, C. Fan, X. Xi, X. Yang, J. Zhang, X. Wang and X. Wu, An FeP@C nanoarray vertically grown on graphene nanosheets: an ultrastable Li-ion battery anode with pseudocapacitance-boosted electrochemical kinetics, *Nanoscale*, 2019, **11**: 1304-1312.

18   F. Liu, L. Wang, Z. Zhang, P. Shi, Y. Feng, Y. Yao, S. Ye, H. Wang, X. Wu and Y. Yu, A mixed lithium-ion conductive Li_2S/Li_2Se protection layer for stable lithium metal anode, *Adv. Funct. Mater.*, 2020, **30**: 2001607.

19   R. Wang, J. Yu, J. Tang, R. Meng, L. F. Nazar, L. Huang and X. Liang, Insights into dendrite suppression by alloys and the fabrication of a flexible alloy-polymer protected lithium metal anode, *Energy Storage Mater.*, 2020, **32**: 178-184.